Optical Materials 62 (2016) 438–446

Contents lists available at ScienceDirect

Optical Materials

journal homepage: www.elsevier.com/locate/optmat

# Structural properties and visible emission of $Eu^{3+}$-activated $SiO_2$–ZnO–$TiO_2$ powders prepared by a soft chemical process

M.P.S. Almeida [a, b], L.M. Nunes [a], R.R. Gonçalves [c], S.J.L. Ribeiro [d], L.J.Q. Maia [e, *]

[a] Instituto de Química - UFG, Campus II, C.P. 131, CEP 740001-970, Goiânia, GO, Brazil
[b] Instituto Federal de Educação, Ciência e Tecnologia - Goiás, Parque Itatiaia, CEP 74968-755, Campus Aparecida de Goiânia, GO, Brazil
[c] Departamento de Química, Faculdade de Filosofia, Ciências e Letras de Ribeirão Preto, USP, Av. Bandeirantes, 3900, CEP 14040-901, Ribeirão Preto, SP, Brazil
[d] Departamento de Química Geral e Inorgânica, Instituto de Química, UNESP, C.P. 355, CEP 14801-970, Araraquara, SP, Brazil
[e] Instituto de Física - UFG, Campus II, C.P.131, CEP 74001-970, Goiânia, GO, Brazil

ARTICLE INFO

*Article history:*
Received 12 September 2016
Received in revised form
15 October 2016
Accepted 18 October 2016
Available online 24 October 2016

*Keywords:*
Europium ion
Photoluminescence
$SiO_2$–ZnO–$TiO_2$ system
Powder
Soft chemical process

ABSTRACT

In this work, the structural and optical properties of the $60SiO_2$–$20ZnO$–$20TiO_2$ system (in mol%) doped with 1 mol% of $Eu^{3+}$ were evaluated. Stable and transparent sols, homogeneous gels, and powders were prepared by a soft chemical process followed by annealing from 700 to 1100 °C. Visible emission was observed in the photoluminescence (PL) spectra from 570 to 700 nm owing to the $Eu^{3+}$ ions, with the most intense emission peaks at 614 and 590 nm related to the $^5D_0 \rightarrow {}^7F_2$ and $^5D_0 \rightarrow {}^7F_1$ transitions, corresponding to red (R) and orange (O) colors, respectively. The R/O intensity ratios between 3.16 and 3.73 were observed and correlated to the structural properties of the host. X-ray diffraction patterns indicated that the reduction of PL at 614 nm and changes in the R/O values were due to the crystallization process. In addition, the FTIR spectra showed a gradual decrease of the hydroxyl absorption bands around 3436 and 1640 $cm^{-1}$ and an increase of the bands related to Ti–O–Ti and Si–O–Si linkages, indicating polymerization and densification process of the host was achieved above 700 °C. Moreover, increasing the annealing temperature resulted in the formation of $ZnTiO_3$ and $Zn_2TiO_4$ crystalline phases, as well as rutile $TiO_2$. Finally, intensity parameters ($\Omega_\lambda$), and quantum efficiency were calculated by applying Judd–Ofelt theory to $Eu^{3+}$ ions, which showed that the $Eu^{3+}$-doped samples can be used in displays and LEDs.



## 1. Introduction

Lanthanide ion ($Ln^{3+}$)-doped inorganic luminescent materials have become an important topic of research in nanoscience and nanotechnology [1]. The optical properties of lanthanide ion-doped silicate systems are of great interest for fundamental studies and technological applications in optical devices, such as lasers, fiber amplifiers, and waveguides. Therefore, a detailed understanding of the local structure and bonding of dopant cations is important for optical device engineering [2].

The ZnO–$TiO_2$ binary system is commonly studied and can be obtained using different oxide combinations, synthesis processes, and thermal treatments, and can be doped with transition metal ions to obtain luminescent materials [3,4]. In this binary system, various crystalline phases are normally formed, such as $Zn_2Ti_3O_8$, $ZnTiO_3$ (zinc metatitanate), and $Zn_2TiO_4$ (zinc orthotitanate). As shown in chemical Equations (1) and (2), $Zn_2Ti_3O_8$ is metastable and forms at low temperatures (<820 °C), whereas between 820 and 950 °C, unstable $ZnTiO_3$ and $TiO_{2(r)}$ (rutile $TiO_2$) are formed. However, the unstable $ZnTiO_3$ phase decomposes into stable $Zn_2TiO_4$ and $TiO_{2(r)}$ phases around 950 °C. The stable $Zn_2TiO_4$ crystalline structure is highly energetically favorable and can be easily obtained by solid-state [5], which requires high temperatures to form the desired phases, and normally generates inhomogeneous and large particle sizes.

$ZnTiO_3$ and $Zn_2TiO_4$ have been doped with transition metals and their luminescent properties have been studied [3,4]. The crystal structure of these compounds can have two types of defects, and the dopant ions can be included in interstitial or substitutional sites. In particular, $ZnTiO_3$ shows photoluminescence at room

* Corresponding author.
*E-mail address:* lauro@ufg.br (L.J.Q. Maia).

http://dx.doi.org/10.1016/j.optmat.2016.10.032
0925-3467/

temperature, due to the oxygen vacancies defects [6,7].

$$Zn_2Ti_3O_3 \xrightarrow{< 820^{\circ}C} 2ZnTiO_3 + TiO_{2(r)} \quad (1)$$

$$2ZnTiO_3 \xrightarrow{> 950^{\circ}C} Zn_2TiO_4 + TiO_{2(r)} \quad (2)$$

The $SiO_2$–ZnO binary system commonly forms $Zn_2SiO_4$ (zinc orthosilicate or willemite) at high temperatures and the sol-gel process is frequently used to obtain nanocrystalline powders. In this system, silicon and oxygen tetrahedra, called orthosilicates $(SiO_4)^{4-}$, are covalently linked, and zinc is associated with the oxygen of the tetrahedra through ionic interactions between $Zn^{2+}$ and $(SiO_4)^{4-}$ [8]. He et al. [9] showed that heating at temperatures higher than 900 °C favors reaction between $SiO_2$ and ZnO to form $Zn_2SiO_4$, which have been explored as phosphors when doped with rare-earth ions or transition metal. For example, when doped with manganese ions ($Mn^{2+}$) can emit in the green region. Zinc orthosilicate and zinc titanate compounds obtained from binary systems exhibit interesting optical, electronic, and photoluminescence (PL) emission [3,7].

The incorporation of ZnO and/or $TiO_2$ increase the refractive index of silicate compounds and the solubility of rare-earth ions is expected, also higher in comparison with that of the pure silica, which has a low rare-earth solubility of $10^{18}$ ions/cm$^3$ [10,11]. It would be a breakthrough enabling not only the miniaturization of optoelectronic and photonic devices, but also improving rare-earth ions solubility in silica derived host. ZnO usually has an undefined stoichiometry, caused by either excess metal ($Zn_{1+x}O$) or oxygen deficiencies ($ZnO_{1-x}$) in the ZnO crystal structure. ZnO can generate defects in the silica network acting as modifier and breakdown Si-O-Si linkages, allowing the formation of non-bonding oxygens (Si-O$^-$). The non-bonding oxygens can even coordinate $Eu^{3+}$ ions allowing their greater dispersion into the host [9,12].

There are not many reports in the literature on the $SiO_2$–ZnO–$TiO_2$ ternary system. In 1975, Holland and Segnit [13] studied this ternary system, which contains a ZnO-rich phase, to evaluate the equilibrium between the liquid and solid phases. More recently, Sava and collaborators [14] used structural characterization of $SiO_2$–ZnO–$TiO_2$ ternary system obtained by the sol-gel method to evaluate the effect of parameters, such as pH, temperature, and catalyst, on phase formation. Subsequently, Irimpan et al. [15] evaluated the non-linear optical properties of a 5 mol% ZnO-doped $SiO_2$–$TiO_2$ binary system and observed that the refractive index and non-linear absorption increase as the volume fraction of ZnO increases. However, none of the ternary materials in these previous studies were doped with rare-earth ions or phosphors, nor were the optical properties studied with a focus on display applications.

Based on their high chemical and thermal stability, the $SiO_2$–ZnO–$TiO_2$ materials are very interesting due to their applications in toxic waste management, chemical protection coatings, and dielectric layers in optoelectronics, solid electrolytes, catalysts, and especially in developing efficient light-energy conversion systems and optical devices [14–16]. Gels of this ternary system can be used for some applications such as toxic wastes incorporation, but in others are required powders as catalysts and source for physical depositions, and thin films for chemical protections and displays. When the physical methods are used, a source of the ceramic or compacted powder material form should be employed to produce homogeneous thin films of complex materials. On the other hand, if a chemical method is used, it is interesting to use very stable and non-toxic sols to produce high quality thin films by dip-coating or spin-coating techniques.

The $SiO_2$-ZnO-$TiO_2$ ternary system choice was based on the properties of crystalline phases and glasses mentioned above and its technological applications. In this study, the synthesis of the ternary system $60SiO_2$–$20ZnO$–$20TiO_2$ (in mol%) doped with 1 mol % of $Eu^{3+}$ was achieved using a mixed methodology (sol-gel process and Pechini method). This method is low cost, does not require atmosphere control, and uses low annealing temperatures to obtain powders. In addition, the structural properties and PL emission spectra were determined as a function of heat-treatment to evaluate the use of these systems as phosphors in displays, and the $Eu^{3+}$ quantum efficiency and Judd–Ofelt parameters were determined. Here, we present only the results for the selected composition ($60SiO_2$–$20ZnO$–$20TiO_2$) as a function of heat-treatment, which shows the most interesting optical and structural features concerning optical devices application.

## 2. Experimental procedures

Sols, gels, and powders of $60SiO_2$–$20ZnO$–$20TiO_2$ (in mol%) doped with 1% mol of $Eu^{3+}$ were prepared. A soft chemical process combining sol-gel and polymeric precursor methodologies was developed to obtain stable and transparent sols. The mixed methodology was based on those used for $SiO_2$–ZnO and $SiO_2$–$TiO_2$ binary systems in the literature [9,17].

The molar ratio between citric acid (CA), acting as a chelating agent, and ethylene glycol (EG), acting as a polymerizing agent, was 3:2. The same molar ratio between metal citrates and EG was proposed by Pechini [18] for polyesterification reactions. The molar ratio between CA and the metal cations (MC) was 3:1. In accordance with Neves et al. [19], this molar ratio allows the formation of stable metallic citrate. The tetraethyl orthosilicate (TEOS) was used as silica precursor. Thus, the molar ratio of CA:EG:TEOS:MC in solution was 3:2:1:1. The synthesis of the sols was achieved using titanium citrate formed by dissolving titanium(IV) isopropoxide ($Ti(OC_3H_7)_4$, Fluka, ≥97.0% purity) in a solution of CA ($C_5O_7H_8 \cdot H_2O$, Sigma-Aldrich, 99.5% purity) in ethanol ($C_2H_5OH$, Chemycalis, 95.0% purity) at 30 °C for 5 min. After homogenization of the solution, europium nitrate pentahydrate ($Eu(NO_3)_3 \cdot 5H_2O$, Aldrich, 99.9% purity) and zinc nitrate hexahydrate ($Zn(NO_3)_2 \cdot 6H_2O$, Vetec, 98.0% purity) were added, and then TEOS ($Si(OC_2H_5)_4$, Merck, >98.0% purity) was added to form Zn–Eu-Ti–citrates. After further homogenization (10 min), EG ($C_2H_4(OH)_2$, Merck, ≥99.5% purity) was added to the metal citrate solution. The gels were obtained by drying the sols at 60 °C over 5 days. Then, the gels were subjected to a heat treatment from 100 to 1100 °C at a heating rate of 5 °C/min heating rate without a holding time to obtain powders for evaluation of the crystallization process.

The optical transmittance and absorbance spectra of the sols were measured using an UV/Vis/NIR spectrophotometer (PerkinElmer WB1050) from 350 to 750 nm using quartz cuvette as sample holder and air as reference.

The sample weight losses over the temperature range of 30–950 °C were determined by thermogravimetric analysis (TG) in a thermobalance (Shimadzu, model DTG-60H) under a continuous flow of synthetic air (50 mL/min) with a heating rate of 10 °C/min, using samples of about 23 mg.

Fourier-transform infrared (FTIR) spectra were recorded in transmission mode on a PerkinElmer spectrometer (model Spectrum 400 FTIR) in the 400–4000 cm$^{-1}$ range using the standard KBr pellet technique. The spectra were obtained out with a resolution of 4 cm$^{-1}$ and a typical normalization procedure was applied.

Unpolarized Raman spectra were collected between 200 and 1200 cm$^{-1}$ at room temperature with a micro-Raman spectrometer (Horiba/Jobin Yvon, HR800) using the backscattering geometry. The powdered samples were excited using a He-Ne laser at 632.8 nm.

X-ray diffraction (XRD) patterns were collected with a Shimadzu

diffractometer (model XRD 6000) operating at 40 kV and 30 mA with Cu $K\alpha$ radiation ($\lambda = 1.54056$ Å). The XRD data were obtained between 10° and 80° (2θ) using a scan rate of 2°/min and an increment of 0.02°.

High-resolution transmission electron microscopy (HR-TEM) images were acquired using a JEOL microscope (model JEM-2100) operating at 200 keV. The program used for the acquisition of planar distances was Gatan Digital Micrograph.

PL excitation and emission spectra of the powders were measured using a Horiba/Jobin Yvon spectrofluorometer (Fluorolog-3 model FL3-221) with fixed slits for 1.0 nm-resolution, a 450 W Xe arc lamp was used as excitation source, and detection was carried out using a Hamamatsu photomultiplier tube. The excitation spectra of samples from 350 nm to 595 nm were collected monitoring emissions at 614 nm, and the emissions spectra between 500 and 750 nm were collected under excitation at 394 nm, in front face mode. $Eu^{3+}$ $^5D_0$ decay times were obtained with a pulsed Xe arc lamp (3 μs bandwidth). The PL emission was corrected for the spectral response of the monochromators and the detector using the typical correction spectrum provided by the manufacturer. All measurements for the samples were carried out at room temperature.

## 3. Results and discussions

### 3.1. Thermal and structural properties

In Fig. 1(a) shows digital photos of the sol as prepared, the dried gel at room temperature, and dried gels and powders heat-treated between 100 °C and 1100 °C. The sol is well transparent between 400 and 750 nm (>71% at 400 nm) with low absorbance (<0.15 at 400 nm), as we can see from transmittance and absorbance spectra in Fig. 1(b). The high absorbance from 350 nm to 400 nm is due to metal-ligand charge-transfer bands and absorptions of organic species. Note that, white color powders could be obtained after heat-treatments from 700 °C to 1100 °C.

Fig. 2 illustrate the TG/DTG curve for the dried gel of $60SiO_2–20ZnO–20TiO_2$ doped with 1 mol% of $Eu^{3+}$. The weight loss stages can be associated with the absorption bands in the FTIR spectra of the same composition presented in Fig. 3. In the TG and DTG curves (Fig. 2), the weight loss stage from 60 to 160 °C is assigned to the elimination of hydrated water and solvent adsorbed

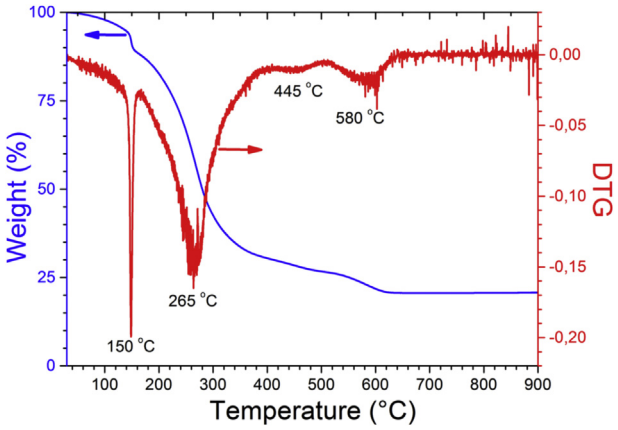


**Fig. 2.** TG and DTG curves of the $60SiO_2–20ZnO–20TiO_2$ gels dried at 60 °C.

on the powder surface. The FTIR spectra obtained in the temperature range of 100–200 °C shows a decrease in the intensity of the band at 1736 $cm^{-1}$ related to the C=O stretching mode of free CA, suggesting that some of the CA is eliminated in this temperature range [20].

The second weight loss stage occurs in the temperature range between 160 and 500 °C (Fig. 2) and can be attributed to the elimination of organic matter and carboxyl groups bonded to ions, corresponding to a weight loss of approximately 70%. In the FTIR spectra (Fig. 3), for powders annealed between 200 and 500 °C, a complete disappearance of the bands at 1736 $cm^{-1}$ (C=O stretching mode of free CA), 2980 and 1376 $cm^{-1}$ (C–H stretching and deformation, respectively), and 1088 $cm^{-1}$ (C–OH axial stretching) was observed [20]. The band at 1634 $cm^{-1}$ overlaps or is coincident with the C=O asymmetric stretching of the carboxylate groups for an unidentate complex and the deformation vibrations of condensing water molecules [21]. In addition, a small inflection is observed in the DTG curve (Fig. 2) in the temperature range between 400 and 500 °C, which coincides with the complete disappearance of the bands in the 2900–3200 $cm^{-1}$ region related to C–H stretching. This observation suggests that the band remaining at 1634 $cm^{-1}$ above 500 °C corresponds to OH groups.

Above 700 °C, a gradual decrease of the hydroxyl absorption

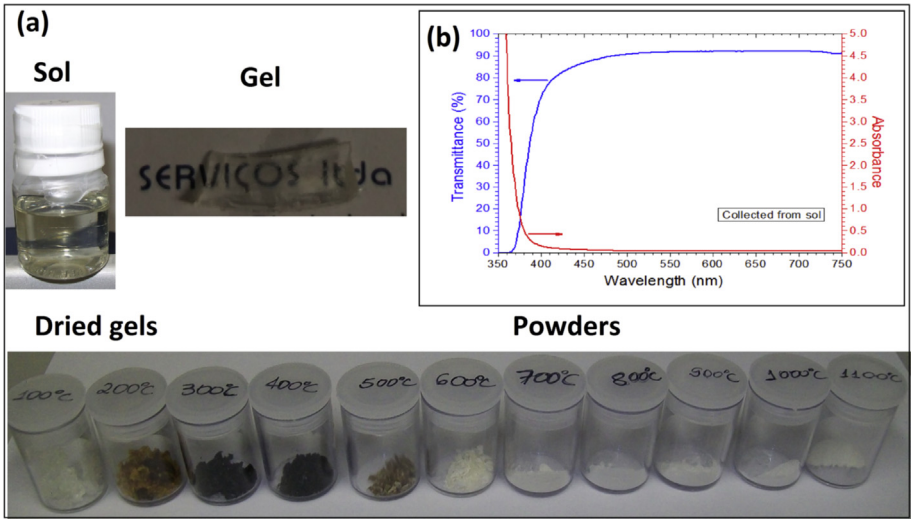


**Fig. 1.** (a) Digital photos of the sol as prepared, the dried gel at room temperature, and the materials (dried gels and powders) heat-treated between 100 °C and 1100 °C. (b) Transmittance and absorbance spectra of the sol.

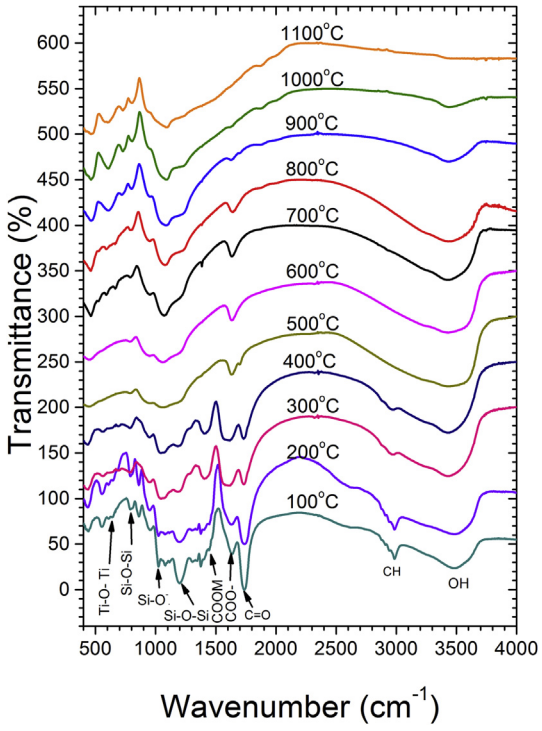


**Fig. 3.** FTIR normalized spectra of $60SiO_2$–$20ZnO$–$20TiO_2$ gels and powders samples annealed from 100 °C to 1100 °C.

bands around 3436 $cm^{-1}$ is observed in the FTIR spectra (Fig. 3), and another pattern is detected in the 800–400 $cm^{-1}$ region corresponding to the absorption bands of Zn–O (450 and 610 $cm^{-1}$), Ti–O (462 and 526 $cm^{-1}$), Ti–O of $TiO_6$ (580 $cm^{-1}$), and Si–O–Ti (900–1000 $cm^{-1}$). At the same temperature, the Raman spectra (Fig. 4) show peaks at 410, 740, and 950 $cm^{-1}$, suggesting the formation of the $ZnTiO_3$ structure [22,23], which is confirmed by the XRD patterns presented below. After annealing at 800 °C, the sample showed FTIR absorption bands at 460, 610, 660, and 780 $cm^{-1}$, which are related to M–O stretching (where M = metal), which is characteristic of spinel-type structures. These observations are in agreement with the XRD diffraction patterns and Raman spectra reported by Chaves et al. [3].

Finally, a decrease in the intensity associated with Si–O–Ti (900–1000 $cm^{-1}$) and an increase in the absorption of new linkages, such as Si–O–Si (800 and 1100–1200 $cm^{-1}$) and Ti–O–Ti (500–600 $cm^{-1}$) are observed in the FTIR spectra (Fig. 3). The Raman spectra for powders heat-treated above 900 °C (Fig. 4) show a structural change, is associated with the beginning of the crystallization of the $Zn_2TiO_4$ phase and segregation of $TiO_2$ as the rutile phase. Such crystallization leads to titanium oxide segregation, as reported by Gunji et al. [24], and will be well discussed below with the XRD results.

The XRD patterns of the powders annealed from 700 to 1100 °C are presented in Fig. 5. At 700 °C, the powder is completely amorphous, whereas the XRD pattern of the powder heat-treated at 800 °C shows peaks characteristic of zinc metatitanate ($ZnTiO_3$, JCPDS card N° 39-0190) [25]. In contrast, the diffraction patterns of the powders heat-treated from 900 to 1100 °C, show a slight shift of the main peaks at 35.4° and 30.0° toward smaller angles, which is indicative of the formation of the $Zn_2TiO_4$ phase (JCPDS card N° 25-1164) [26]. The XRD pattern for the powders heat-treated at 1100 °C reveals a low intensity peak corresponding to an additional phase, the $TiO_2$ rutile structure (JCPDS card N° 88-1175) [27]. The segregation of this oxide occurs concomitantly with the formation of zinc titanate ($Zn_2TiO_4$). The Raman spectra (Fig. 4) confirms the presence of the $TiO_2$ rutile phase in the powder heat-treated at 900 °C or higher.

Both zinc titanate phases have numerous similarities in their crystallographic cards; however, the phases obtained are consistent with those reported in the literature for the ZnO–$TiO_2$ binary system [28,29]. In this system, the $Zn_2Ti_3O_3$ phase decomposes to $ZnTiO_3$ and $TiO_2$ rutile phases at temperatures below 820 °C, but at temperatures higher than 950 °C, the $ZnTiO_3$ phase transforms into $Zn_2TiO_4$ and $TiO_2$ rutile phases. The main peak of the $TiO_2$ rutile phase had a very low intensity, and was not easily observed in the diffractograms collected at 2.0°/min. However, when the XRD pattern was collected at 0.5°/min (inset, Fig. 5), the main diffraction peak of the $TiO_2$ rutile phase at 27.6° was clearly observed, confirming the assignment of the phases in the Raman spectra in Fig. 4. The powders had crystallite sizes of 9.0 and 19.0 nm at 900 and 1100 °C, respectively.

TEM images show that the sample does not have crystalline structures at 700 °C. The material remained amorphous up to a temperature of 800 °C, where crystallization began and spherical nanoparticles with an average size of 5.4 ± 0.1 nm were observed (Fig. 6(a)). At a temperature of 900 °C, spherical nanoparticles were

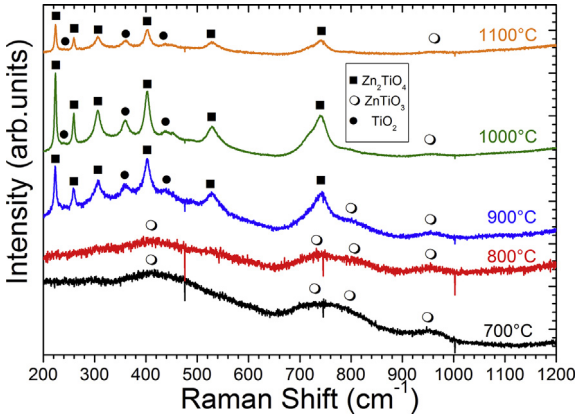


**Fig. 4.** Raman spectra of $60SiO_2$–$20ZnO$–$20TiO_2$ powders samples annealed from 700 °C to 1100 °C.

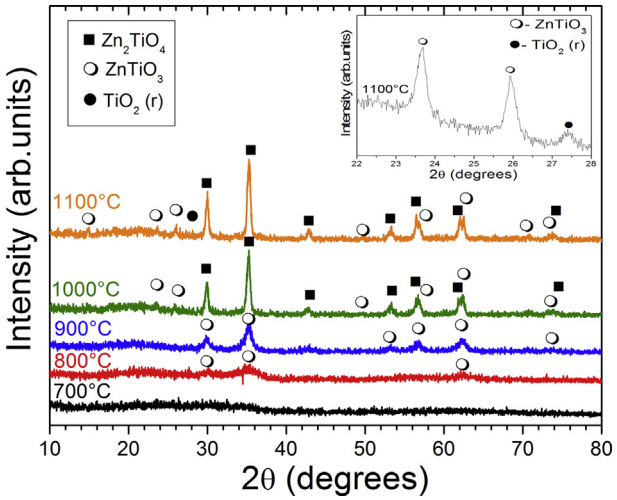


**Fig. 5.** X-ray diffraction patterns of $60SiO_2$–$20ZnO$ - $20TiO_2$ powders annealed at different temperatures, and the inset is of that heat-treated at 1100 °C.

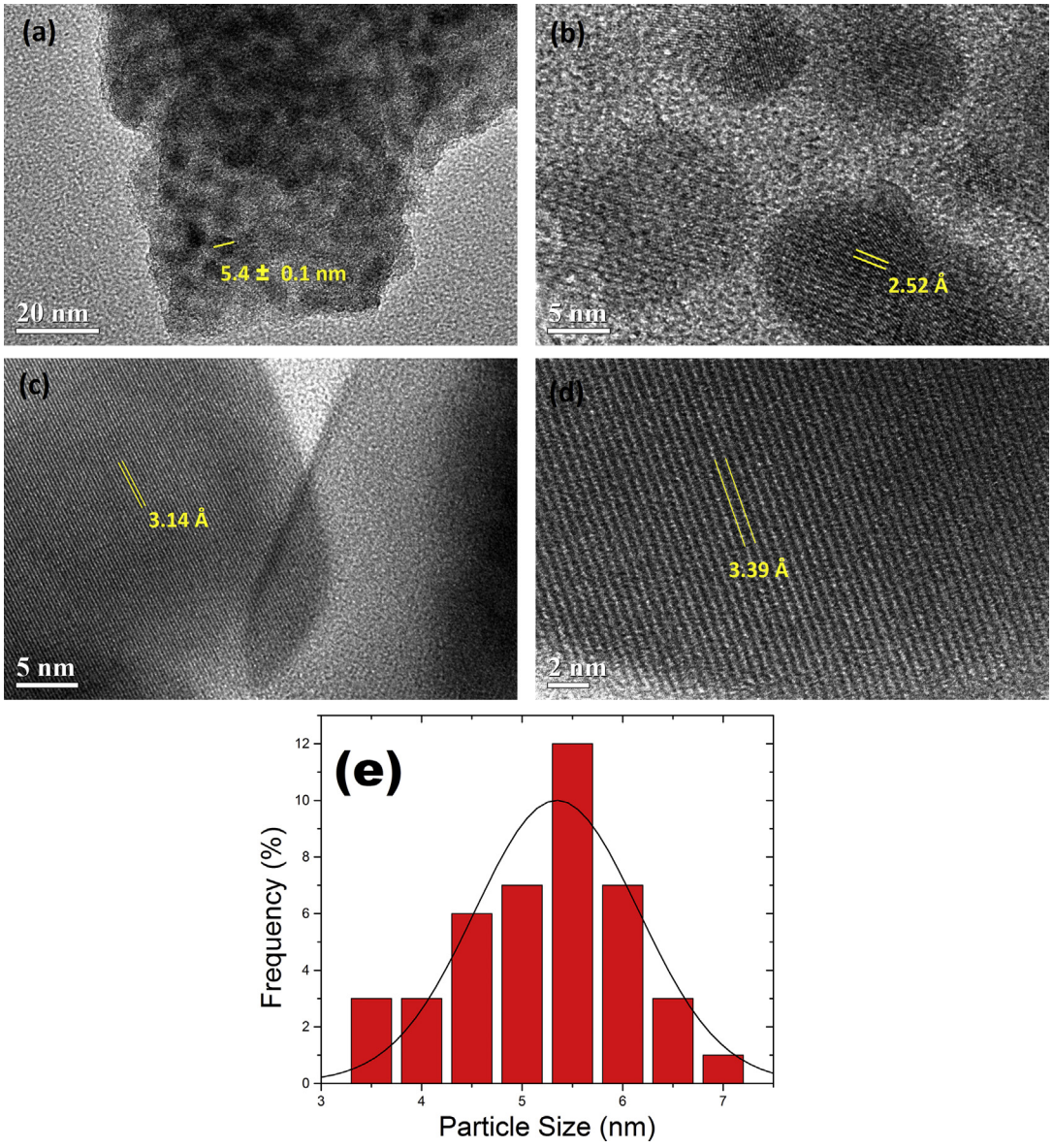


**Fig. 6.** TEM image of powders with $60SiO_2$–$20ZnO$–$20TiO2$, treated at a) 800 °C; b) 900 °C; c) 1000 °C; d) 1100 °C and e) statistical histogram of the size distribution of the nanoparticles of Fig. 5a.

observed to be dispersed in an amorphous medium (Fig. 6(b)), with an interatomic distance of ~2.54 ± 0.05 Å, which corresponds to the (311) plane of $ZnTiO_3$ [24]. Planar distances of 3.14 ± 0.04 Å (Fig. 6(c)) and 3.39 ± 0.05 Å (Fig. 6(d)) were measured for the powders heat treated at 1000 and 1100 °C, which are similar to that expected for the (220) plane of the $Zn_2TiO_4$ phase and the (110) plane of the $TiO_2$ rutile phase, respectively [25,26]. These images corroborate the data obtained by XRD. Fig. 6(e) shows a statistical histogram of the narrow size distribution of the nanoparticles in Fig. 6(a).

The zinc titanate compounds obtained here are consistent with those observed by Chang et al. [5]. However, in our work, the crystallization of $Zn_2Ti_3O_8$, as proposed by Yang and Swisher [30] and Kim et al. [31], was not observed, probably due to modification of the phase formation kinetics by the used chemical process.

Many reports on the synthesis of binary ZnO–$TiO_2$ indicate that different compounds can be formed simultaneously [4,32]. Hou et al. [22] used the sol-gel process to prepare compounds with a 1:1 mol ratio of ZnO and $TiO_2$, and obtained a mixture of crystalline phases from 800 to 1000 °C, as elucidated by XRD. However, in these systems, crystalline compounds were already observed around 500 °C, whereas the silica present in our ternary system increases the crystallization temperature. Gunji et al. [24] reported that silica retarded titanium oxide segregation in a $SiO_2$–$TiO_2$ binary system. On the other hand, Aubert et al. [33] reported the formation of ZnTiO crystallites with an unidentified ratio at temperatures higher than 600 °C, showing that $Eu^{3+}$ doped thin films showed high red emission when annealed at 800 °C. The various zinc titanate structures have been evaluated by researchers. In 1960, Dulin and Rase [34] proposed a phase diagram for the ZnO–$TiO_2$ binary system, and recently, Yang and Swisher [30] and Kim et al. [31] have included new structures in the phase diagram, specifically $Zn_2Ti_3O_8$. Our FTIR, Raman, and XRD results showed that despite the presence of $SiO_2$ led to phase crystallization as indicated in the phase diagram proposed by Kim et al. [31].

### 3.2. $Eu^{3+}$ ion excitation and emission

Fig. 7(a) shows the excitation spectra from $60SiO_2$-$20ZnO$-$20TiO_2$ (mol%) powders doped with 1 mol% of $Eu^{3+}$ heat-treated (H.T.) from 700 °C to 1100 °C. The narrow bands around 362, 382, 394, 413, 464, 533, and 579 nm are attributed to the *f-f* transitions of the $Eu^{3+}$ $4f^6$ configuration. These peaks are assigned to the transitions $^7F_0 \rightarrow {}^5D_4$ (362 nm), $^7F_0 \rightarrow {}^5G_{2\text{-}6}$ (382 nm), $^7F_0 \rightarrow {}^5L_6$ (394 nm), $^7F_0 \rightarrow {}^5D_3$ (414 nm), $^7F_0 \rightarrow {}^5D_2$ (464 nm), $^7F_0 \rightarrow {}^5D_1$ (533 nm), and $^7F_0 \rightarrow {}^5D_0$ (579 nm). For powders H.T. between 700 °C and 900 °C the strongest peak is located at 394 nm, but those ones H.T. at 1000 °C and 1100 °C the strongest peak is centered at 464 nm. In fact, increasing the temperature of heat-treatment, the intensity peak at 464 nm in comparison with that at 394 nm increases, indicating that the $Eu^{3+}$ surroundings have been changed. Another feature is observed for $^7F_0 \rightarrow {}^5D_0$ transition, which is not only at 579 nm, but also another narrow and centered at 587 nm for H.T at 1100 °C; and a broadening is observed for powders H.T. from 700 °C to 1000 °C, probably mainly due to two different microenvironments for $Eu^{3+}$ ions. It is reasonable suppose that the $ZnTiO_3$ and $Zn_2TiO_4$ lattices distorts to have enough space for extra oxygen accommodation and this extra oxygen in the lattices could be responsible for another $Eu^{3+}$ transition $^7F_0 \rightarrow {}^5D_0$ (at 587 nm). Only 394 nm excitation was chosen to achieve emission spectra due to its dominant intensity in most samples.

Fig. 7(b) shows the emission spectra of $Eu^{3+}$ excited at 394 nm for $60SiO_2$–$20ZnO$–$20TiO_2$ as a function of annealing temperature (from 700 to 1100 °C). The observed emissions are due to $^5D_0 \rightarrow {}^7F_0$ (578 nm), $^5D_0 \rightarrow {}^7F_1$ (591 nm), $^5D_0 \rightarrow {}^7F_2$ (614 nm), $^5D_0 \rightarrow {}^7F_3$ (652 nm), and $^5D_0 \rightarrow {}^7F_4$ (701 nm) transitions, and the dominant emission occurs for the electric dipole allowed transition around 614 nm.

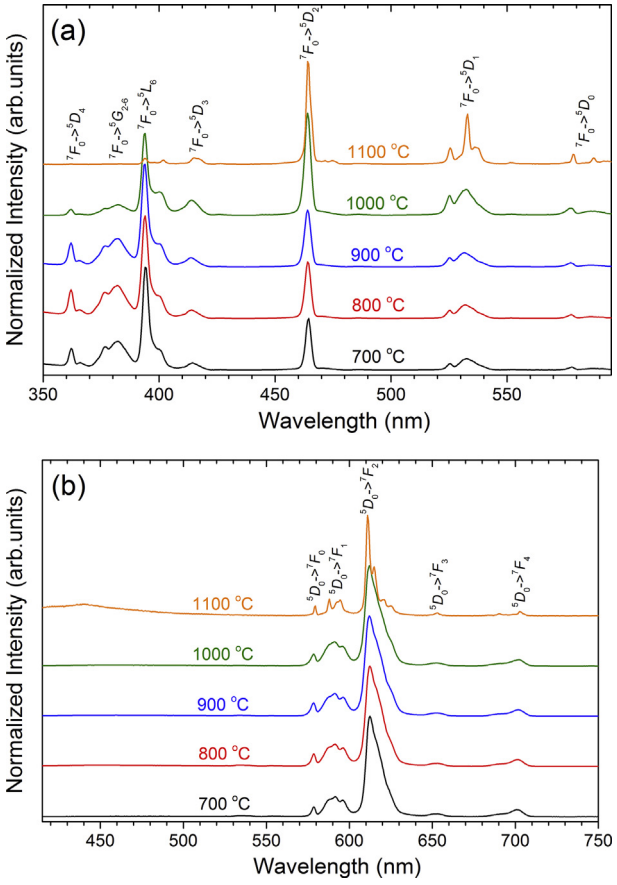


**Fig. 7.** $Eu^{3+}$ room-temperature (a) excitation spectra (emission wavelength 614 nm) and (b) emission spectra (excitation wavelength 394 nm) of $60SiO_2$–$20ZnO$–$20TiO_2$ powders samples annealed from 700 °C to 1100 °C, doped with 1 mol% of $Eu^{3+}$.

Yaiphaba et al. [1] mention that the splitting levels depend on the (i) intensity of the excitation source; (ii) excitation/emission slit widths; and (iii) crystallinity. At high annealing temperatures (at 900 and at 1000 °C), the energy levels do not split, as expected due to the high sample crystallinity, and similarity regarding the distribution of $Eu^{3+}$ ions, which are located in similar regions or sites. On the other hand, although the annealing temperature can result in organization around active ions, defects around the ions can decrease the PL emission. In addition, $Eu^{3+}$ ion segregation can occur to form Eu–O–Eu clusters, which leads to energy transfer between adjacent $Eu^{3+}$ ions, and defects can quench the PL emission [35]. Stark splitting is well observed only for sample H.T. at 1100 °C, related to $Eu^{3+}$ ions located in crystalline sites, also a broad band centered at 440 nm was noted in this sample, probably from defects in the host.

The characteristics of the PL spectra shown in Fig. 7(b) and the crystallization process are directly related to changes in the R/O values (Table 1). The R/O value is the relation between the emission intensities at 614 and 590 nm due to the $^5D_0 \rightarrow {}^7F_2$ and $^5D_0 \rightarrow {}^7F_1$ transitions of $Eu^{3+}$, respectively. R is red emission (614 nm) corresponding to the electric-dipole-allowed transition and O is orange emission (590 nm) corresponding to the magnetic-dipole-allowed transition [36]. At 700 °C, the samples have R/O values of around 3.55, indicating low symmetry around the $Eu^{3+}$ ions. However, at 900 °C changes occur due to the effective crystallization of some phases in the powders, and the R/O value is around 3.73, indicating an even more asymmetric environment around $Eu^{3+}$. Subsequently, because of the crystalline transition of the material, the R/O values decreases to 3.27 at 1000 °C and to 3.16 at 1100 °C.

Fig. 8 shows the emission decay profiles of the samples annealed between 700 and 1100 °C. The $^5D_0$ decay time was obtained from the profiles with an excitation wavelength of 394 nm and an emission wavelength of 614 nm. As shown in Fig. 8, non single-exponential decays were observed for all of the samples. In this case, the average lifetime can be calculated by Refs. [11,37]:

$$\tau_{avg} = \int_{t_o}^{t_f} \frac{I(t)}{I_o} dt, \tag{3}$$

where $\tau_{avg}$ is the average lifetime, $I(t)$ is the PL intensity at time $t$, $I_o$ is the initial PL intensity at 0 ms, and $t_f$ is the time at which the PL emission becomes zero (~10 ms). The average lifetimes ($\tau_{Avg}$) for the samples annealed between 700 and 1100 °C varied from 1.99 to 1.11 ms, as listed in Table 1.

As the decay profiles were not single-exponential curves, all five curves in Fig. 8 could be fitted to the sum of two exponential functions [38]:

**Table 1**
R/O ratio values between $^5D_0 \rightarrow {}^7F_2$ and $^5D_0 \rightarrow {}^7F_1$ transitions and the average decay lifetime in milliseconds of $^5D_3 \rightarrow {}^7F_2$ transition of $Eu^{3+}$ ions in $60SiO_2$–$20ZnO$–$20TiO_2$ in mol% powders annealed from 700 °C to 1100 °C.

| Heat-treatment (°C) | R/O ratio | Average lifetime ($\tau_{Avg}$) (±0.05 ms) |
|---|---|---|
| 700 | 3.55 | 1.99 |
| 800 | 3.70 | 1.82 |
| 900 | 3.73 | 1.59 |
| 1000 | 3.27 | 1.24 |
| 1100 | 3.16 | 1.11 |

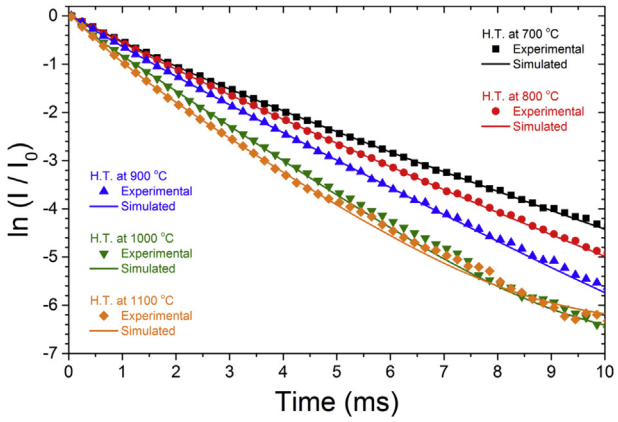


**Fig. 8.** $Eu^{3+}$ room-temperature emission decay curves monitored at 614 nm under excitation at 394 nm obtained for $60SiO_2$–$20ZnO$–$20TiO_2$ powder samples annealed from 700 °C to 1100 °C. Lines show fits obtained with two adjusted decay times and amplitudes $A_1$ and $A_2$ ($A_1 + A_2 = 1$), respectively. For 700 °C, $\tau_1 = 2.46$ ms, $\tau_2 = 1.11$ ms, $A_1 = 0.64$ and $A_2 = 0.36$; for 800 °C, $\tau_1 = 2.11$ ms, $\tau_2 = 1.09$ ms, $A_1 = 0.71$ and $A_2 = 0.29$; for 900 °C, $\tau_1 = 1.75$ ms, $\tau_2 = 0.71$ ms, $A_1 = 0.83$ and $A_2 = 0.17$; for 1000 °C, $\tau_1 = 1.37$ ms, $\tau_2 = 0.22$ ms, $A_1 = 0.85$ and $A_2 = 0.15$; and for 1100 °C, $\tau_1 = 1.40$ ms, $\tau_2 = 0.53$ ms, $A_1 = 0.61$ and $A_2 = 0.39$.

$$I = A_1 e^{-t/\tau_1} + A_2 e^{-t/\tau_2}, \tag{4}$$

where $A_1$ and $A_2$ are the amplitudes at zero time, and the sum of $A_1$ and $A_2$ is unity ($A_1 + A_2 = 1$), $I$ is the amplitude at time t, and $\tau_1$ and $\tau_2$ are the decay lifetimes. The values of the decay lifetimes and the amplitudes at zero time are show as a function of heat-treatment in Table 2.

The $A_1$ and $A_2$ values, as well as the $\tau_1$ and $\tau_2$ decay times, varied with the annealing temperature. Increasing the temperature from 700 to 1100 °C resulted in a decrease in the $\tau_1$ value from 2.46 to 1.40 ms and a similar decrease in the $\tau_2$ value from 1.11 to 0.53 ms. This result can be correlated with the differences in the symmetry of the microenvironment or nearest neighbor environment of the rare-earth ion, as well as refractive index changes [39], as observed by Ferrari et al. [40] in $Er^{3+}$-doped $SiO_2$–$Ta_2O_5$. The increase in $A_1$ from 700 to 1000 °C indicated that $Eu^{3+}$ ions are preferentially incorporated in Zn sites of the $ZnTiO_3$ phase, likely because the ionic radius of $Eu^{3+}$ (1.066 Å) is closer to that of $Zn^{2+}$ (0.74 Å) than that of $Ti^{4+}$ (0.68 Å) [41,42]. However, the formation of the $Zn_2TiO_4$ and $TiO_2$ rutile phases at higher temperatures decreases the $A_1$ amplitude, while increasing $\tau_1$, suggesting that the formation of $Zn_2TiO_4$ and rutile $TiO_2$ reduces the $^5D_0$ lifetime of $Eu^{3+}$. All these features are corroborated by XRD patterns presented in Fig. 5, or be powders remained amorphous until 700 °C, increasing the heat treatment causes an increase of the crystalline content and its crystallinity (formation of $TiO_2$, $Zn_2TiO_4$ and $ZnTiO_3$ phases) which certainly increase the interaction and an efficient energy transfer within the nearest-neighbor $Eu^{3+}$ ions, increasing nonradiative recombination effects. Moreover, some amounts of $Eu^{3+}$ ions can be quenched due to trapped surface defects and structural defects leading to reduction of the excited state radiative lifetime [38–40]. Besides, higher amounts of crystalline contents increase the refractive index of the material that lead to lower radiative lifetime of $Eu^{3+}$ ions, for example, Chang et al. [38] related the lower decay lifetime with the $YInGe_2O_7$ phase formed when the annealing temperature rises. Here in our work, we have a mixture of two crystalline phases making difficult correlate the lifetime values to a specific phase.

**Table 2**
Decay lifetimes and the amplitudes at zero time of $^5D_3 \rightarrow {}^7F_2$ transition of $Eu^{3+}$ ions in $60SiO_2$–$20ZnO$–$20TiO_2$ in mol% powders annealed from 700 °C to 1100 °C.

| Temperature (°C) | $\tau_1$ (ms) | $\tau_2$ (ms) | $A_1$ | $A_2$ |
|---|---|---|---|---|
| 700 | 2.46 | 1.11 | 0.64 | 0.36 |
| 800 | 2.11 | 1.09 | 0.71 | 0.29 |
| 900 | 1.75 | 0.71 | 0.83 | 0.17 |
| 1000 | 1.37 | 0.22 | 0.85 | 0.15 |
| 1100 | 1.40 | 0.53 | 0.61 | 0.39 |

In the study on $R_{3-3x}Eu_{3x}SbO_7$ (R = La, Gd or Y, x = 0.05–1.0) synthesized *via* a solid state reaction [37], the authors reveal a pair broadening effect for intermediate $Eu^{3+}$ doping ($0.2 < x \leq 0.6$, lifetime of ~1.2 ms in $La_{2.40}Eu_{0.60}SbO_7$), in a heavily $Eu^{3+}$-doped sample ($0.7 \leq x \leq 1.0$, lifetime of ~0.2 ms in $La_{0.90}Eu_{2.10}SbO_7$) there are cluster centers inducing luminescence quenching, and only for low concentrations ($0.05 \leq x \leq 0.2$, lifetime of ~2.3 ms in $La_{2.85}Eu_{0.15}SbO_7$) there are isolated $Eu^{3+}$ centers. Note that 1 mol% of $Eu^{3+}$ correspond to x = 0.0133 ($La_{2.96}Eu_{0.04}SbO_7$) should have only isolated centers. Based on this, we can propose that our samples have similar behavior, at low H.T. temperatures there are isolated centers and at higher H.T. temperatures present pair broadening effect and clustering formation.

Werts et al. [43] and Carlos et al. [44] previously calculated the spontaneous emission probability ($A$), radiative lifetime ($\tau_{Rad}$), quantum efficiency for $^5D_0 \rightarrow {}^7F_2$ emission, and $\Omega_2$ and $\Omega_4$ parameters, as presented below.

The pure magnetic-dipole character of the $^5D_0 \rightarrow {}^7F_1$ transition enables the determination of the intensity parameters from the emission spectrum. As this transition does not depend on the local ligand field experienced by $Eu^{3+}$ ions, it can be used as a reference for the entire spectrum [43,44]. The $A_{01}$ spontaneous decay rate for the $^5D_0 \rightarrow {}^7F_1$ transition is $A_{01} = A'_{01} \cdot n^3$, where $A'_{01} = 14.65\ s^{-1}$ in vacuum and $n$ is the refractive index of the host material. Then, the intensity of the $^5D_0 \rightarrow {}^7F_{0\text{-}6}$ transitions in terms of the area of the emission curves ($S_{0J}$) is:

$$S_{0J} = h c \bar{\upsilon} A_{0J} N(5_{D0}), \tag{5}$$

where $N(^5D_0)$ is the $^5D_0$ level population that emits. The total radiative decay rate can be written as:

$$A_T = \sum_{J=0}^{6} A_{0J} = \frac{A_{01} h c \upsilon_{01}}{S_{01}} \sum_{J=0}^{6} \frac{S_{0J}}{h c \upsilon_{0J}} \tag{6}$$

The branching ratio for the $^5D_0 \rightarrow {}^7F_{5,6}$ transitions must be neglected owing to its low relative intensity, and the radiative contribution can be calculated using only the $^5D_0 \rightarrow {}^7F_{0\text{-}4}$ transitions [44].

The emission quantum efficiency ($q$) is defined by the experimental and radiative lifetime ratio:

$$q = \frac{\tau_{Avg}}{\tau_{Rad}} \tag{7}$$

The site symmetry and luminescence behavior of $Eu^{3+}$ ions in the matrix was carried out by calculating the Judd–Ofelt parameters $\Omega_\lambda$ ($\lambda = 2, 4$). In the Judd–Ofelt theory, the intensity parameters $\Omega_\lambda$ are given by:

$$\Omega_\lambda = \frac{3h}{64\pi^4 e^2 \bar{\upsilon}^3} \frac{9}{n(n^2+2)^2} \frac{1}{\left|\left\langle 5D0 \middle| U^{(\lambda)} \middle| 7FJ \right\rangle\right|^2} A_{0J} \tag{8}$$

The values for the reduced matrix elements are 0.0032 for $\lambda = J = 2$ and 0.0023 for $\lambda = J = 4$. Table 3 lists the determined $A_{01}$, $A_{02}$, $A_{04}$, $A_T$, $\tau_{Rad}$, $q$(%), $\Omega_2$, and $\Omega_4$ values. For comparison, the

**Table 3**
Judd-Ofelt parameters, quantum efficiency, and intensity parameters for $^5D_0$ state under excitation at 394 nm.

| Heat-treatment (°C) | $A_{01}$ ($s^{-1}$) | $A_{02}$ ($s^{-1}$) | $A_{04}$ ($s^{-1}$) | $A_T$ ($s^{-1}$) | $\tau_{Rad}$ (ms) | $\tau_{Avg}$ (ms) | Q (%) | $\Omega_2$ ($10^{-20}$ $cm^2$) | $\Omega_4$ ($10^{-21}$ $cm^2$) |
|---|---|---|---|---|---|---|---|---|---|
| 700 | 55.1 | 204.3 | 14.7 | 274.1 | 3.65 | 1.99 | 55 | 6.27 | 6.44 |
| 800 | 57.6 | 221.5 | 14.6 | 293.7 | 3.40 | 1.82 | 53 | 6.44 | 6.10 |
| 900 | 62.1 | 241.5 | 14.1 | 317.7 | 3.15 | 1.59 | 51 | 6.50 | 5.45 |
| 1000 | 68.4 | 233.5 | 16.0 | 317.9 | 3.14 | 1.24 | 39 | 5.65 | 5.58 |
| 1100 | 68.3 | 224.9 | 15.4 | 308.6 | 3.24 | 1.11 | 34 | 5.44 | 5.34 |

emission quantum efficiency was calculated using the $\tau_{avg}$ values. In this calculation, we used the refractive index ($n$) previously determined for thin films with same the composition and heat-treatment.

The dependence of the radiative lifetime on the heat-treatment originates from the radiation field polarization of the medium and the photon density change in an optically dense medium. In fact, the refractive index varies due to the formation of crystalline phases [45]. The oscillator strength of the electric dipole transition for $Eu^{3+}$ should increase from 700 to 1000 °C, and due to this, the $^5D_0$ radiative lifetime of $Eu^{3+}$ decreases or the radiative transition rates are higher, as seen in Table 3. In this way, the quantum efficiency ($q$) of the $^5D_0 \rightarrow {}^7F_2$ transition is higher for samples heat-treated at 700 °C (55%), but slightly reduced by increasing the heat-treatment to 900 °C (51%), taking into account $\tau_{avg}$. Taking into account the two experimental lifetimes obtained at 900 °C by fitting the decay curve to a bi-exponential function, $q$ values of 56% and 23% are obtained for $\tau_1$ and $\tau_2$, respectively. This result indicates that a high portion of $Eu^{3+}$ ions is located in a protected site that is not well coupled to hydroxyl groups or defects.

The polarization and asymmetry behavior of rare-earth ligands are determined by the $\Omega_2$ parameter, whereas $\Omega_4$ depends on long-range effects [46]. The higher $\Omega_2$ value for $Eu^{3+}$ in samples heat-treated at 900 °C indicates a highly asymmetric nature, which is corroborated by the R/O ratio of 3.73, which is probably related to the formation of a single $ZnTiO_3$ phase. The low $\Omega_4$ value implies that $^5D_0 \rightarrow {}^7F_2$ transition efficiency increases, and this transition accounts for the majority of $Eu^{3+}$ emission, resulting in this material having almost pure red emission.

## 4. Conclusions

Homogeneous and transparent solutions of $60SiO_2$–$20ZnO$–$20TiO_2$ doped with 1 mol% of $Eu^{3+}$ were prepared by a mixed methodology consisting of a sol-gel process and a polymeric precursor method. The structural evolution of the gels and powders were evaluated, with effective removal of organic compounds at annealing temperatures between 600 and 700 °C, and the residual hydroxyl groups removed at higher annealing temperatures, especially 1100 °C. The crystalline phases obtained depending on the annealing temperature, with zinc titanate ($Zn_2TiO_4$) as the major phase as high temperatures. However, at 800 °C, only $ZnTiO_3$ is formed. At 900 °C, the largest R/O ratio was obtained as a consequence of the low symmetry around $Eu^{3+}$ ions in the crystallized $ZnTiO_3$ phase. Moreover, this sample had good quantum efficiency (55% and 23% for $\tau_1$ and $\tau_2$ or 51% for $\tau_{avg}$). $Eu^{3+}$ ions in the $60SiO_2$–$20ZnO$–$20TiO_2$ host system have a high $\Omega_2$ value, revealing their highly asymmetric nature, which depends on the annealing temperature and the crystalline phases. Finally, interesting structural characteristics and optical emission were obtained for $Eu^{3+}$-doped samples with potential application in displays as nanostructured red emitters.

## Acknowledgements

The authors would like to thank the Brazilian agencies CNPq, CAPES, FAPEG, FAPESP, IFG, and FUNAPE for financial support, and PhD student Robson Rosa Silva of UNESP-Araraquara for help with Raman spectra measurements.

## References

[1] N. Yaiphaba, R.S. Ningthoujam, N. Shanta Singh, R.K. Vatsa, N. Rajmuhon Singh, J. Lumin 130 (2010) 174–180.
[2] C. Zhu, A. Monteil, M. El-Jouad, N. Gaumer, S. Chaussedent, Opt. Lett. 34 (2009) 3749–3751.
[3] A.C. Chaves, S.J.G. Lima, R.C.M.U. Araújo, M. Aldeiza, M.A. Maurera, E. Longo, P.S. Pizani, L.G.P. Simões, L.E.B. Soledade, A.G. Souza, I.M.G. Santos, J. Sol. St. Chem. 179 (2006) 985–992.
[4] S.F. Wang, M.K. Leu, F. Gu, C.F. Song, D. Xu, D.R. Yuan, G.J. Zhou, Y.X. Qi, Inorg. Chem. Commun. 6 (2003) 185–188.
[5] Y.S. Chang, Y.H. Chang, I.G. Chen, G.J. Chen, Y.L. Chai, T.H. Fang, S. Wu, Ceram. Int. 30 (2004) 2183–2189.
[6] J. Mrázek, G. Krylova, A. Brioude, S. Ababou-Girard, L. Spanhel, Phys. Chem. Chem. Phys. PCCP 12 (2010) 15101–15110.
[7] C. Ye, Y. Wang, Y. Ye, J.Z. Hang, G.H. Li, J. Appl. Phys. 106 (2009) 1–4.
[8] M.R. Davolos, A.M. Pires, Chem. Mater 13 (2001) 21–27.
[9] H. He, Y. Wang, Y. Zou, J. Phys. D. Appl. Phys. 36 (2003) 2972–2975.
[10] T.T. Van, J.P. Chang, Appl. Phys. Lett. 87 (2005), 011907-1–;011907–3.
[11] L.J.Q. Maia, V.R. Masteralo, A.C. Hernandes, J. Fick, A. Ibanez, Thin Solid Films 517 (2009) 6584–6587.
[12] D.C. Look, D.C. Reynolds, R.L. Jones, D.B. Eason, Appl. Phys. Lett. 81 (2002) 1830–1832.
[13] A.E. Holland, E.R. Segnit, Aust. J. Chem. 28 (1975) 2373–2376.
[14] B.A. Sava, A. Diaconu, M. Elisa, C.E.A. Grigorescu, I.C. Vasiliu, A. Manea, Superlattice Microstr. 42 (2007) 314–321.
[15] L. Irimpan, B. Krishnan, V.P.N. Nampoori, P. Radhakrishnan, Opt. Mater 31 (2008) 361–365.
[16] B.A. Sava, Rev. Chim. 55 (2004) 220–223.
[17] L.L. Yang, Y.S. Lai, J.S. Chen, P.H. Tsai, C.L. Chen, C. Chang, J. Mater. Res. 20 (2005) 3141–3149.
[18] M.P. Pechini. U.S. Patent nº 3 (1967) 330–697.
[19] P.P. Neves, L.J.Q. Maia, M.I.B. Bernardi, A.R. Zanatta, V.R. Mastelaro, J. Sol-Gel Sci. Technol. 29 (2004) 89–96.
[20] R.A. Rocha, E.N.S. Muccillo, Cerâmica 47 (2001) 219–224.
[21] G.B. Deacon, R.J. Phillips, J. Coord. Chem. Rev. 33 (1980) 227–250.
[22] L. Hou, Y.D. Hou, M.K. Zhu, J. Tang, J.B. Liu, H. Wang, H. Yan, Mater. Lett. 59 (2005) 197–200.
[23] H. Beigi, V.H. Bindu, H.Z.R. Hamoon, K.V. Rao, J. Nano-Electron. Phys. 3 (2011) 47–52.
[24] T. Gunji, T. Kasahara, Y. Abe, J. Sol-Gel Sci. Technol. 13 (1998) 975–979.
[25] JCPDS - Joint Committee for Powder Diffraction Standards, File. N°. 39–0190.
[26] JCPDS - Joint Committee for Powder Diffraction Standards, File. N°. 25–1164.
[27] JCPDS - Joint Committee for Powder Diffraction Standards, File. N°. 88–1175.
[28] C.L. Wang, W.S. Hwang, K.M. Chang, H.H. Ko, C.S. Hsi, H.H. Huang, M.C. Wan, Int. J. Mol. Sci. 12 (2011) 935–945.
[29] N.T. Nolan, M.K. Seery, S.C. Pillai, Chem. Mater 23 (2011) 1496–1504.
[30] J. Yang, J.H. Swisher, Mater. Charact. 37 (1996) 153–159.
[31] H.T. Kim, Y. Kim, M. Valant, D. Suvorov, J. Am. Ceram. Soc. 84 (2001) 1081–1086.
[32] C. Li, Y. Bandoa, M. Nakamuraa, N. Kimizukal, H. Kito, Mater. Res. Bull. 35 (2000) 351–358.
[33] T. Aubert, F. Grasset, M. Potel, V. Nazabal, T. Cardinal, S. Pechev, N. Saito, N. Ohashi, H. Haneda, Sci. Technol. Adv. Mater. 11 (2010) 1–9.
[34] F.H. Dulin, D.E. Rase, J. Am. Ceram. Soc. 43 (1960) 125–131.
[35] L. Rebohle, W. Skorupa, Rare-earth Implanted MOS Devices for Silicon Photonics, first ed., Springer Series in Materials Science, Berlin, 2010.
[36] Z. Wang, J. Wang, H. Zhang, Mater. Chem. Phys. 87 (2004) 44–48.
[37] J. Wang, Y. Cheng, Y. Huang, P. Cai, S.I. Kim, H.J. Seo, J. Mater. Chem. C (2014) 5559–5569.
[38] Y.S. Chang, J. Electron. Mater. 37 (2008) 1024–1028.
[39] E. Snoeks, A. Lagendijk, A. Polman, Phys. Rev. Lett. 74 (1995) 2459–2462.

[40] J.L. Ferrari, K.O. Lima, L.J.Q. Maia, S.J.L. Ribeiro, A.S.L. Gomes, R.R. Gonçalves, J. Nanosci. Nanotechnol. 11 (2011) 2540–2544.
[41] Y.V. Kolenko, K.A. Kovnir, A.I. Gavrilov, A.V. Garshev, P.E. Meskin, B.R. Churagulov, M. Bouchard, C. Colbeau-Justin, O.I. Lebedev, G. Van Tendeloo, M. Yoshimura, J. Phys. Chem. B 109 (2005) 20303–20309.
[42] W. Luo, R. Li, G. Liu, M.R. Antonio, X. Chen, J. Phys. Chem. C 112 (2008) 10370–10377.
[43] M.H.V. Werts, R.T.F. Jukes, J.W. Verhoeven, Phys. Chem. Chem. Phys. 4 (2002) 1542–1548.
[44] L.D. Carlos, R.A.S. Ferreira, V. Zea Bermudez, S.J.L. Ribeiro, Adv. Mater. 21 (2009) 509–534.
[45] G. Pan, H. Song, Q. Dai, R. Qin, X. Bai, B. Dong, L. Fan, F. Wang, J. Appl. Phys. 104 (2008) 0849101–0849109.
[46] S. Som, A.K. Kunti, V. Kumar, V. Kumar, S. Dutta, M. Chowdhury, S.K. Sharma, J.J. Terblans, H.C. Swart, J. Appl. Phys. 115 (2014) 1931011–19310114.